Earth, Planets and Space

FULL PAPER Open Access

# Estimation of weak and strong ground motions based on diffuse field concept for earthquake for steps 2 and 3 of blind prediction exercise

Fumiaki Nagashima[1*], Hiroshi Kawase[1], Kenichi Nakano[2] and Eri Ito[1]

**Abstract**

For the accurate prediction of earthquake ground motions, the investigation of three elements in its process, namely the source, path, and site effects, is crucial, and their accuracy and reliability should be evaluated. The Committee of the 6th Effect of Surface Geology on Seismic Motion Symposium conducted a blind prediction exercise to investigate the accuracy and reliability of estimating the subsurface velocity structure related to the site effect and for predicting weak and strong ground motions. We participated in a blind prediction exercise and estimated the weak and strong ground motions that occurred during the 2016 Kumamoto earthquake sequence. First, the velocity structures at a target site KUMA and our reference site EEB were identified based on the diffuse field concept for earthquake (DFCe). The identified velocity structures at KUMA and EEB reproduced the observed horizontal-to-vertical spectral ratios of earthquakes well and were considered to be able to reproduce the horizontal and vertical site amplification factors based on DFCe. Second, the incident waves at the seismic bedrock of EEB were estimated. For weak and strong ground motions, the spectral amplitudes of the three components of the incident waves were estimated from the vertical motions observed on the surface at EEB assuming the generation of a diffuse field for a single earthquake record and the linearity of the vertical amplification factor, even during strong shaking. Finally, the ground motions on the surface at KUMA were estimated using the incident waves estimated at the seismic bedrock, the inverted velocity structure, and the dynamic deformation characteristics distributed by the organizer of the blind prediction exercise for shallow soil sediments. The spectral amplitudes of the estimated strong ground motions were smaller at around 1 Hz and larger at around 10 Hz than the observed ones. However, the estimated overall spectral levels of all components corresponded to the observed ones. Although several parameters require further research, such as the damping factor of soil sediments, we have shown that the proposed method can estimate the overall seismic ground motions at a target site in the blind.

**Keywords** Ground motion estimation, Blind prediction, Diffuse field, Horizontal-to-vertical spectral ratio, Seismic bedrock

*Correspondence:
Fumiaki Nagashima
nagashima@sds.dpri.kyoto-u.ac.jp
Full list of author information is available at the end of the article

## Graphical Abstract

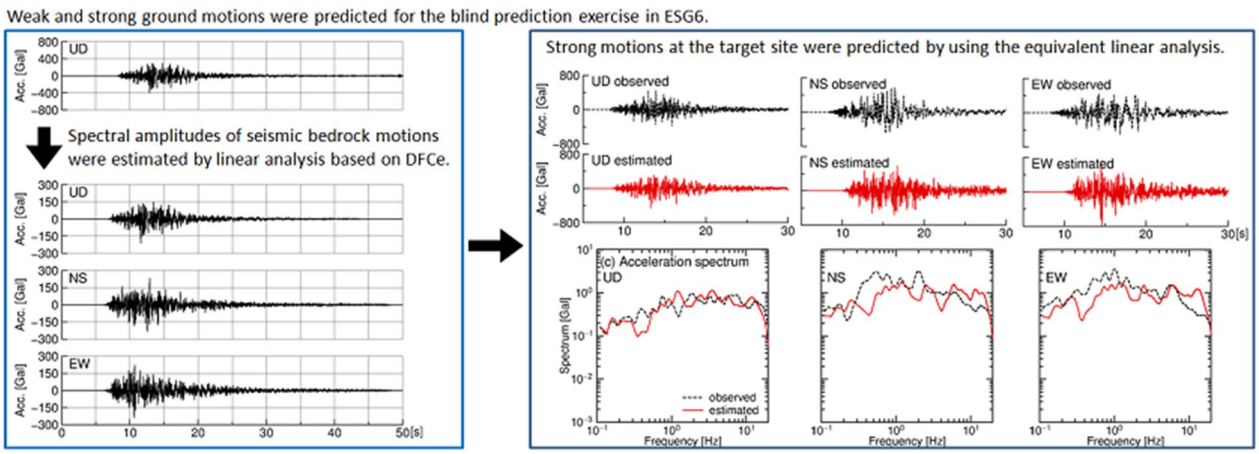


## Main text

### Introduction

In estimating the ground motions at a specific site, there are many choices for the parameters, such as the source of the ground motions, Q values of the path, subsurface velocity structure, and nonlinear dynamic properties of the soil. There are also choices for estimation methods, such as source rupture representation (e.g., Irikura and Miyake 2011), the deconvolution analysis of earthquake records (e.g., Satoh et al. 1995; Giuseppe et al. 2014); the analysis of wave propagation in subsurface structures considering linear, equivalent linear, or nonlinear behavior (e.g., Graves and Pitarka 2016; Chiara et al. 2011); and effective-stress analysis considering the effect of pore-water pressure (e.g., Fukutake et al. 1990).

Selecting suitable properties and methods based on a priori information is necessary for reasonable estimations. Expert knowledge regarding the target site and the purpose of the estimation is also helpful. The selection by experts resulted in advantages, such as the optimized combination of parameters and methods and the consideration of the applicable limitations of the parameters and methods. However, the expert decision also introduces uncertainty in the selection. Therefore, the degree of the uncertainty of the prediction and the degree of the impact of the parameters and methods on the uncertainty would be evaluated.

A Joint Working Group on Effect of Surface Geology on Seismic Motion (JWG-ESG) stimulated discussions during the international symposium on ESG about this uncertainty by conducting a series of blind prediction exercises and simultaneous simulations. ESG1 was the first symposium on ESG and was held in 1992 in Odawara, Japan. Blind prediction experiments were conducted to identify the one-dimensional velocity structure of the Turkey Flat, USA, and Ashigara Valley, Japan. ESG2 was held in 1998 in Yokohama, Japan, during which a simultaneous simulation of strong ground motion during the 1995 Kobe earthquake, Japan, was conducted. ESG3 was held in 2006 in Grenoble, France, during which a blind test was conducted to investigate the reliabilities of dispersion curves and inverted share-wave profiles, and to simulate nonlinear behavior and a 3D basin response (e.g., Cornou et al. 2006). Besides blind predictions in ESG, blind tests focusing on the site effect derived from microtremors were performed in the Site Effects Assessment Using Ambient Excitations (SESAME) (e.g., Bard and SESAME participants 2004). Régnier et al (2016, 2018) reported results of the PREdiction of NOn-LINear soil behavior (PRENOLIN) project which was performed to verify variations due to the equivalent linear/nonlinear ground motion estimation codes and to validate the estimated waveforms. Asten et al. (2022) presented results from the Consortium of Organizations for Strong Motion Observation Systems (COSMOS) blind trials which focused on site characterization derived from microtremors.

At ESG6, held in 2021, a blind prediction exercise for structural inversion and the prediction of weak and strong ground motions at a private site was conducted. The exercise comprised three steps: Step 1 was the identification of the subsurface structure using microtremor records (Chimoto et al. 2021, 2023), Step 2 was the simulation of weak ground motion during a small earthquake, and Step 3 involved the simulation of strong ground motions considering soil nonlinearity

(Tsuno et al. 2021a, 2021b, 2023). The target earthquakes in Step 2 were the aftershocks of the 2016 Kumamoto earthquake with a JMA magnitude of 5.9, and the target earthquakes in Step 3 were the foreshock and mainshock of the 2016 Kumamoto earthquake. The foreshock occurred on April 14, 2016, Japan Standard Time (JST), with a JMA magnitude of 6.5, and the mainshock occurred on April 16, 2016, with a JMA magnitude of 7.3. The foreshock and mainshock were located along the Futagawa and Hinagu fault zones. Thus, the target earthquakes in Steps 2 and 3 were crustal earthquakes. The 2016 Kumamoto earthquake sequence caused heavy damage around fault zones, and many surface ruptures were observed. Several observation sites have recorded strong motions close to the fault during the mainshock, and the reproduction and interpretation of the near-fault records are now of interest from the perspective of source and site effects. The aim of the blind prediction exercise in ESG6 was not only to evaluate the performance of the latest estimation schemes and their uncertainties by comparing them, but also to conduct blind prediction throughout the entire process: from velocity structure identification to strong motion estimation. Another purpose was to evaluate the variety among the estimated results with incomplete a priori information. In Step 3, the waveform of the mainshock at the reference site provided by the ESG6 blind prediction committee was truncated in the middle of the S-wave because of the power failure; thus, the participants had options for the input motions for the strong motion estimation.

We participated in a blind prediction exercise in ESG6 at all steps. In this study, the ground motion predictions of a small earthquake (Step 2) and strong motion predictions (Step 3) are reported. The diffuse field concept for earthquakes (DFCe; Kawase et al. 2011, Nagashima et al. 2014, Nagashima and Kawase 2022) was adopted to identify the subsurface velocity structure and estimate the input motions. The ground motions at the target site named KUMA (Matsushima et al. 2021, 2023) were estimated using linear and equivalent linear analyses in Steps 2 and 3, respectively. The committee distributed earthquake records at a site in a mountainous area named SEVO as a reference site; however, the mainshock record was truncated after the S-wave arrival because of power failure. Thus, instead of SEVO, earthquake records at a site named EEB, a seismic intensity meter (Shindokei) site installed by the Japan Meteorological Agency (JMA) closest to KUMA, were used to estimate the input motions. The locations of the sites and the epicenters of the target earthquakes are shown in Fig. 1. The distance between EEB and KUMA was approximately 1.2 km.

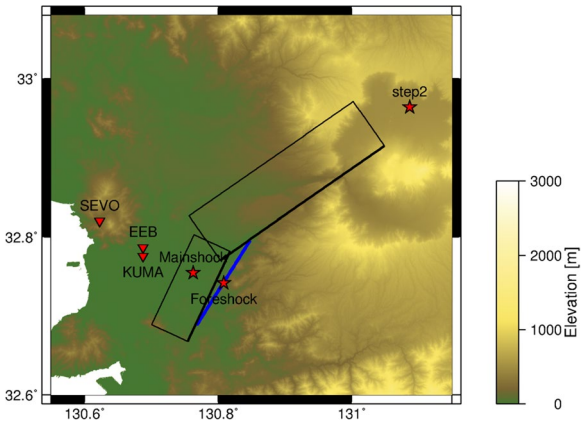


**Fig. 1** Locations of KUMA, EEB, SEVO and epicenters of the target earthquake of Step 2 and 3. The blue and black rectangles show the fault models of the foreshock and mainshock of the 2016 Kumamoto earthquake (Asano and Iwata, 2016, downloaded from SRCMOD)

#### Identification of subsurface velocity structures

First, the subsurface velocity structures at KUMA and EEB were inverted from the horizontal-to-vertical spectral ratios of earthquake (EHVR) based on DFCe (Kawase et al. 2011; Nagashima et al. 2014).

In obtaining the observed EHVR, earthquake waveforms of 40 s from the S-wave onset were extracted, the cosine shape taper of 1 s was applied to both ends of the waveforms, spectral amplitudes were calculated by Fast Fourier Transform and smoothed using a Parzen window with a band width of 0.1 Hz, the ratios of North–South (NS) over Up-Down (UD) components and those of East–West (EW) over UD components of each earthquake were calculated, and the geometrical means of NS/UD and EW/UD among the earthquakes were taken. The waveforms of 12 earthquakes distributed by the blind prediction committee were used to calculate the observed EHVR at KUMA, and 16 earthquake records provided by the JMA were used to calculate the observed EHVR at EEB. The earthquake parameters are listed in Tables 1 and 2. The calculated EHVRs are shown in Fig. 2. Both EHVRs have a peak at 0.3–0.4 Hz and a broad peak at 1.0 Hz. The difference between NS/UD and EW/UD was small, suggesting 1D horizontal layering at both sites (Matsushima et al. 2014).

The observed EHVRs were inverted to identify the velocity structures based on DFCe. According to DFCe, the EHVR is interpreted as the ratio of the horizontal amplification factor and the vertical amplification factor with the coefficients of the S-wave and P-wave velocities (Vs and Vp) at a seismic bedrock as follows:

**Table 1** Earthquakes used to calculate the observed EHVR at KUMA

| Date | $M_{JMA}$ | PGA-NS [Gal] | PGA-EW [Gal] | PGA-UD [Gal] |
|---|---|---|---|---|
| 2016/04/16 01:05 | 3.3 | 4.8 | 6.9 | 3.3 |
| 2016/04/16 04:05 | 4.0 | 39.5 | 35.7 | 34.9 |
| 2016/04/16 07:23 | 4.8 | 37.7 | 64.3 | 40.4 |
| 2016/04/16 11:02 | 4.4 | 48.1 | 99.2 | 27.5 |
| 2016/04/17 00:14 | 4.8 | 28.1 | 14.3 | 10.4 |
| 2016/04/17 04:46 | 4.5 | 23.0 | 26.1 | 15.4 |
| 2016/04/17 19:23 | 4.4 | 20.2 | 15.2 | 11.1 |
| 2016/04/18 08:35 | 4.2 | 11.3 | 12.1 | 6.1 |
| 2016/04/21 21:52 | 4.0 | 19.9 | 25.2 | 14.6 |
| 2016/05/05 10:31 | 4.6 | 13.7 | 11.3 | 5.4 |
| 2016/05/05 10:40 | 4.9 | 13.2 | 14.9 | 5.0 |
| 2016/05/19 02:37 | 3.9 | 13.4 | 23.5 | 13.2 |

$$\frac{H(f)}{V(f)} = \sqrt{\frac{\alpha}{\beta}} \frac{\left|TF_{horizontal}(f)\right|}{\left|TF_{vertical}(f)\right|}, \quad (1)$$

where H(f) and V(f) represent the Fourier spectra of the horizontal and vertical components, respectively. TF is the transfer function on the surface due to the vertically incident wave at the seismic bedrock; thus, $|TF_{horizontal}(f)|$ and $|TF_{vertical}(f)|$, which are the absolute values of TF, are the horizontal and vertical amplification factors between the seismic bedrock and ground surface. α and β are Vp and Vs at a seismic bedrock, respectively. To obtain optimized velocity structure models, we minimized the residuals between the observed EHVR and theoretical EHVR in Eq. 1 by using the Hybrid Heuristic Searching method (HHS), a combination of a real-type genetic algorithm and an annealing simulation (Yamanaka 2007). The detailed conditions for the inversion are as follows:

- The initial model for both sites consisted of 19 layers and half-space bedrock. If the number of layers is too small, the identified structure has a large impedance contrast, and the peak and dip of the theoretical EHVR become higher and smaller than that of the observed EHVR, respectively. Thus, the number of layers was sufficiently large to reproduce the shape of the EHVR.

**Table 2** Earthquakes used to calculate the observed EHVR at EEB

| Date | $M_{JMA}$ | PGA-NS [Gal] | PGA-EW [Gal] | PGA-UD [Gal] |
|---|---|---|---|---|
| 2012/08/17 08:46 | 4.9 | 7.9 | 6.1 | 6.4 |
| 2014/08/29 04:14 | 6.0 | 7.5 | 9.1 | 9.4 |
| 2015/07/13 02:52 | 5.7 | 20.9 | 18.8 | 16.9 |
| 2015/08/26 07:51 | 5.2 | 4.1 | 3.3 | 3.1 |
| 2015/11/14 05:51 | 7.1 | 3.3 | 4.8 | 4.6 |
| 2016/03/03 16:11 | 4.9 | 1.8 | 1.8 | 1.5 |
| 2016/04/15 05:10 | 4.6 | 35.6 | 45.8 | 35.9 |
| 2016/04/16 03:03 | 5.9 | 21.2 | 35.7 | 37.2 |
| 2016/04/16 03:55 | 5.8 | 33.7 | 41.9 | 25.8 |
| 2016/04/16 14:03 | 4.6 | 2.1 | 3.7 | 3.2 |
| 2016/04/16 14:27 | 4.6 | 30.2 | 37.2 | 41.8 |
| 2016/04/18 20:42 | 5.8 | 19.0 | 42.1 | 34.2 |
| 2016/04/19 17:52 | 5.5 | 34.8 | 32.8 | 32.3 |
| 2016/04/19 20:47 | 5.0 | 38.7 | 34.3 | 24.4 |
| 2016/05/05 10:31 | 4.6 | 9.6 | 13.2 | 12.4 |
| 2016/05/05 10:40 | 4.9 | 13.5 | 22.6 | 24.4 |

- The identified variables were Vs, Vp, and the thickness of the 19 layers.
- The variables were identified without the searching range, but velocity inversion with depth was prohibited; thus, the identified Vs and Vp increased with increasing depth.
- The thickness of the first layer should be larger than the threshold of Vs/4/20, owing to the 1/4 wavelength law at the maximum frequency of interest (20 Hz).
- Damping $h$ and density $\rho$ were converted based on the formulae $h = 2.5/Vs$ and $\rho = 1.4 + 0.67^{*}\mathrm{sqrt}(Vs/1000)$ (Kobayashi et al. 1995), where Vs is in m/s.
- In identifying laterally homogeneous structures, the root mean square value calculated from two horizontal components (RMS) was obtained for each earthquake record, the ratios of the RMS to UD components were taken, and the geometrical mean of the ratios of the RMS/UD was obtained.
- The residuals between the theoretical and observed EHVR of RMS/UD were minimized using the HHS.

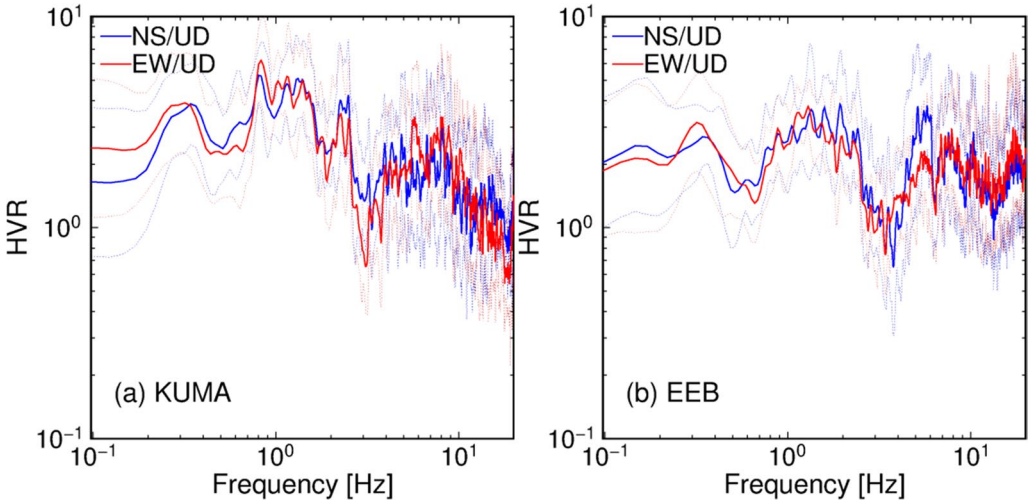


**Fig. 2** Observed EHVR at **a** KUMA and **b** EEB. Solid lines are the geometrical means and dotted lines are averages multiplied/divided by one geometrical standard deviation

- Before inversion, the EHVR was resampled to obtain even frequency increments on a logarithmic scale. The amplitude of the EHVR was also evaluated on a logarithmic scale, and the residuals were evaluated on a log–log scale for frequency and amplitude.
- The residual between the theoretical and observed EHVR was normalized by the sum of the squares of the observed EHVR.
- The residual was calculated in 0.1–20 Hz. To accurately identify deeper structures associated with a fundamental peak at 0.35 Hz, we also calculated the normalized residual in 0.1–0.6 Hz, weighted by being multiplied by six, and minimized together with the normalized residual in 0.1–20 Hz.
- The HHS uses a random number for generating initial models, crossing, mutation, and so on. Thus, inversions were performed 10 times with the same parameter set, but a random number sequence was generated in each inversion. The model with the minimum residual among the 10 inversions was selected as the optimal inversion model.

Figures 3 and 4 show the results of the EHVR inversion at KUMA and EEB, respectively. The detailed velocity profiles of the optimized models are listed in Tables 3 and 4. The inverted structures reproduced the observed EHVR accurately. All 10 inversions converged to similar amplification factors in the horizontal and vertical components, and the 10 inverted velocity structures were similar at each site. Features in common between these two profiles were observed, except for the topmost layers, in which KUMA has a softer and thicker layer than EEB does.

After Step 1 of the blind prediction exercise, the blind prediction committee distributed the phase velocity dispersion curves derived from microtremor records by the participants of the exercise and "the preferred velocity structure model" at KUMA. The preferred model consists of the PS logging data collected at a site close to KUMA for the shallow part (Matsushima et al. 2021, 2023) and the model of Senna et al. (2018) for the deep part. The velocity structure at KUMA identified in this study was validated by comparing it with the dispersion curves and the preferred model (please see Additional file 1). The theoretical phase velocity dispersion curve calculated from the structure identified in this study is slower than the observed curve and the theoretical curve of the preferred model in the frequency range lower than 4 Hz. By contrast, the phase velocity of the preferred model showed good agreement with the observed phase velocity. The structure identified in this study was deeper than the preferred model for reproducing the observed EHVR precisely in the low-frequency range. The theoretical EHVR calculated using the preferred model had a peak near 0.35 Hz but an amplitude smaller than that of the observed EHVR, and the theoretical EHVR did not reproduce the observed EHVR. The structure identified in this study is reasonable for the EHVR, and the preferred model is reasonable for the phase velocity. The discrepancy among the velocity structures identified using different data is a crucial topic; however, this discrepancy is beyond the scope of this study. Notably, the inversion based on DFCe interprets the EHVR as the ratio of the horizontal and vertical amplification factors; thus, DFCe can directly reflect the amplification factor included in the observed data in the identified structure.

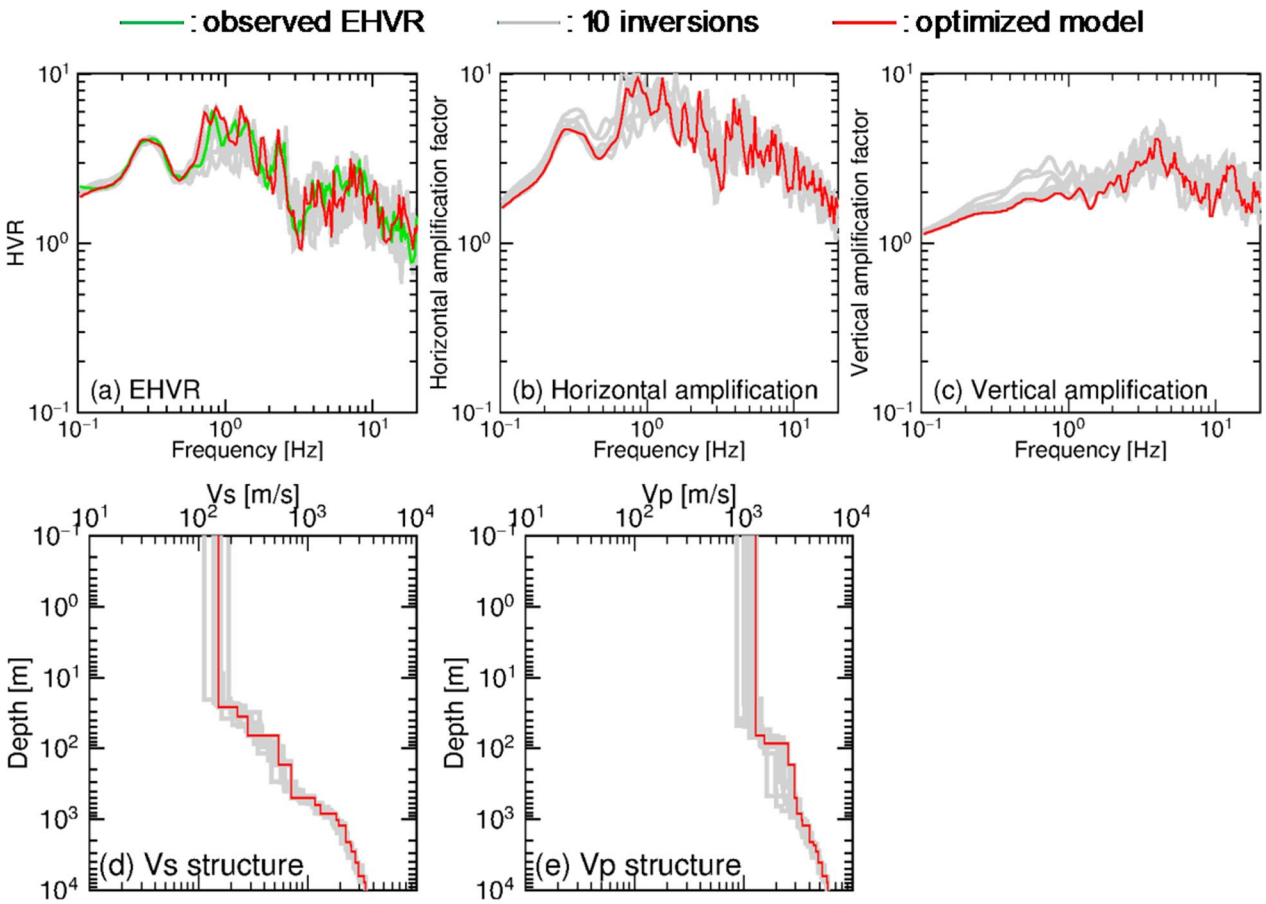


**Fig. 3** Inversion results at KUMA. Green line shows the observed EHVR, gray lines show ten inversions results, and red lines show an optimized model whose residual is minimum among ten inversions. **a** Comparison of the observed EHVR, theoretical EHVRs of ten inverted models and a EHVR of an optimized model. **b** Horizontal amplification factor of ten inverted models. **c** Vertical amplification factors of ten inverted models. **d** Inverted Vs structures. **e** Inverted Vp structures

#### Prediction for a small aftershock

Earthquake motions on the ground surface at KUMA during the small aftershock of the 2016 Kumamoto earthquake sequence were estimated for Step 2 of the blind prediction exercise. The target earthquake of Step 2 occurred on April 16, 2016, JST with a JMA magnitude of 5.9 (Tsuno et al. 2021a, 2023).

To prepare the input motion at KUMA, we first estimated the seismic bedrock motion at EEB on the basis of DFCe (Nagashima and Kawase 2022). Nagashima and Kawase (2022) proposed that the fundamental equation of DFCe (Eq. 1) can be transformed into Eq. 2, which implies that the spectral amplitude of the horizontal incident wave at the seismic bedrock was proportional to that of the vertical component with a coefficient of α and β:

$$\frac{\mathrm{H(f)}}{\left|\mathrm{TF_{horizontal}(f)}\right|} = \sqrt{\frac{\alpha}{\beta}}\frac{\mathrm{V(f)}}{\left|\mathrm{TF_{vertical}(f)}\right|}. \quad (2)$$

If a diffuse field is generated during an earthquake, Eq. 2 holds for a single earthquake record. Assuming the generation of a diffuse field during the target earthquake in Step 2, we estimated the spectral amplitudes of the horizontal and vertical seismic bedrock motions at EEB from the vertical record of EEB by using the right-hand term in Eq. 2. In other words, the spectral amplitude of the horizontal seismic bedrock motion was converted from that of the vertical seismic bedrock motion by multiplying the square root of α over β. Equation 2 was validated by Nagashima and Kawase (2022). The theoretical vertical amplification factor was

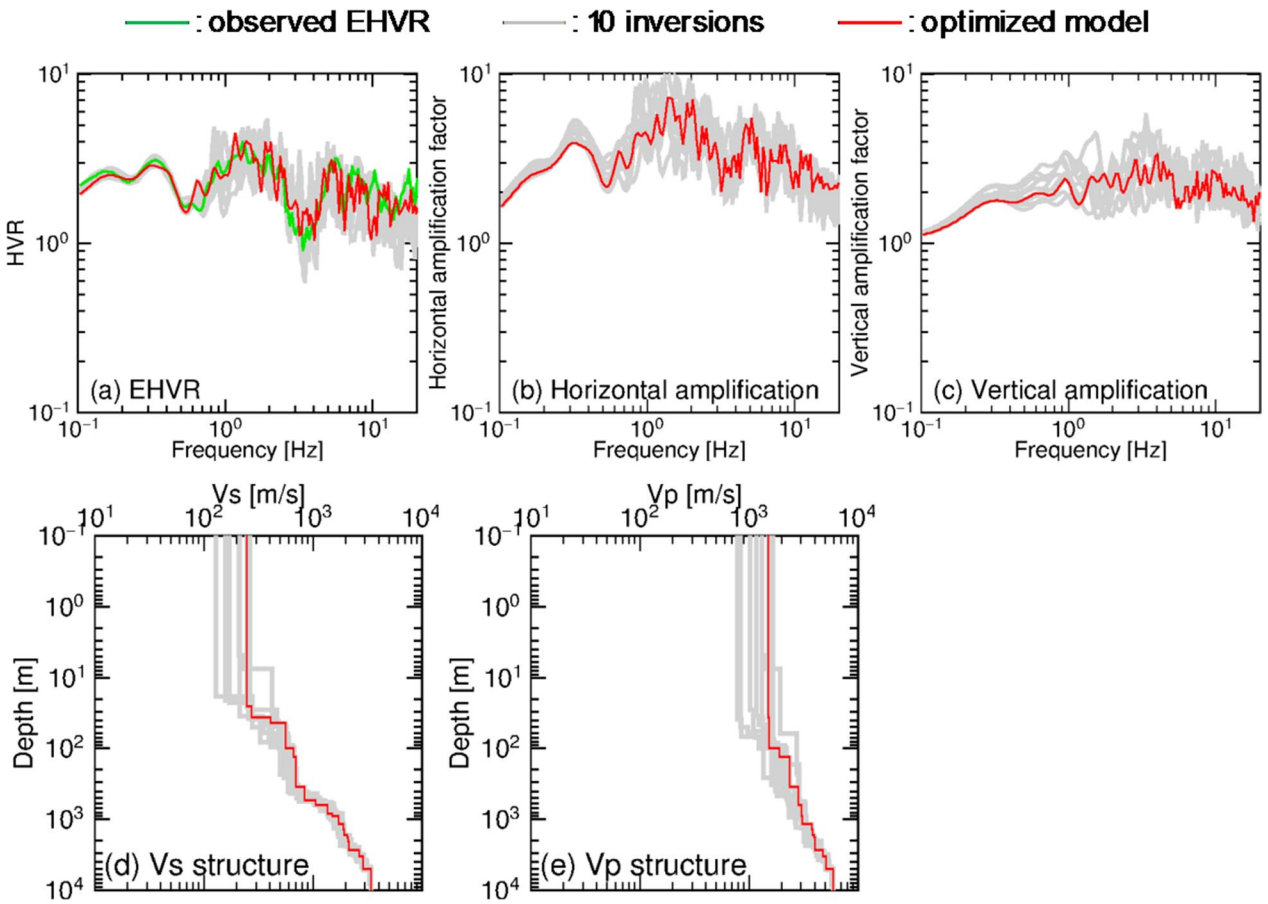


**Fig. 4** Inversion results at EEB. Green line shows the observed EHVR, gray lines show ten inversions results, and red lines show a optimized model whose residual is minimum among ten inversions. **a** Comparison of the observed EHVR, theoretical EHVRs of ten inverted models and a EHVR of a optimized model. **b** Horizontal amplification factor of ten inverted models. **c** Vertical amplification factors of ten inverted models. **d** Inverted Vs structures. **e** Inverted Vp structures

calculated using the velocity structure described in the previous section. Next, the seismic bedrock waves were generated from the estimated spectral amplitudes and the spectral phases of the observed horizontal motions at EEB within the frequency band from 0.1 to 20 Hz. Finally, the unexpected vibration before P-wave arrival, which was caused by insufficient causality between the estimated spectral amplitude and the spectral phase, was tapered by a cosine-shaped function. Considering the locations of KUMA, EEB, and the epicenter of the target earthquake shown in Fig. 1, the source and path terms are in common for KUMA and EEB.

The acceleration waveforms of the target earthquake observed at EEB are shown in Fig. 5. The estimated seismic bedrock motions at EEB are shown in Fig. 6. Figure 6 shows the outcrop motion at the seismic bedrock, which was twice the wave incident on the bedrock. The spectral amplitudes of the NS and EW components of the estimated bedrock motions were calculated from a vertical motion on the surface according to the right-hand term of Eq. 2, and the spectral phases of the NS and EW components were those of the NS and EW components recorded on the surface. Vertical motion at the bedrock was estimated using conventional deconvolution analysis (the spectral amplitude of the vertical bedrock motion was calculated as the spectrum of the vertical record divided by the vertical amplification factor, and the phase of the vertical bedrock motion was one of the vertical components recorded on the surface). The peak ground acceleration (PGA) of the estimated horizontal bedrock motion was approximately one-fifth that of the observed motion on the ground surface, and the vertical motion was approximately two-fifths that of the observed motion on the ground surface.

Using the estimated bedrock waves at EEB and the identified velocity structure at KUMA, the ground motions on the surface at KUMA were predicted by linear soil-response analysis using DYNEQ (Yoshida 2020)

**Table 3** Identified velocity structures at KUMA

| No. | Vs [m/s] | Vp [m/s] | Thickness [m] | Density [kg/m$^3$] | Damping [%] |
|---|---|---|---|---|---|
| 1 | 153 | 1301 | 26 | 1660 | 1.64 |
| 2 | 229 | 1301 | 10 | 1720 | 1.09 |
| 3 | 284 | 1301 | 30 | 1760 | 0.88 |
| 4 | 541 | 1562 | 18 | 1890 | 0.46 |
| 5 | 541 | 2573 | 84 | 1890 | 0.46 |
| 6 | 714 | 2954 | 322 | 1970 | 0.35 |
| 7 | 1178 | 3081 | 136 | 2130 | 0.21 |
| 8 | 1311 | 3081 | 212 | 2170 | 0.19 |
| 9 | 1833 | 3418 | 194 | 2310 | 0.14 |
| 10 | 1931 | 3470 | 189 | 2330 | 0.13 |
| 11 | 2230 | 4025 | 152 | 2400 | 0.11 |
| 12 | 2230 | 4025 | 409 | 2400 | 0.11 |
| 13 | 2230 | 4056 | 325 | 2400 | 0.11 |
| 14 | 2494 | 4382 | 226 | 2460 | 0.10 |
| 15 | 2522 | 4576 | 493 | 2460 | 0.10 |
| 16 | 2723 | 4805 | 1037 | 2510 | 0.09 |
| 17 | 2734 | 4866 | 260 | 2510 | 0.09 |
| 18 | 2956 | 5278 | 2127 | 2550 | 0.08 |
| 19 | 3320 | 5794 | 1534 | 2620 | 0.08 |
| 20 | 3400 | 6000 | – | 2640 | 0.07 |

**Table 4** Identified velocity structures at EEB

| No. | Vs [m/s] | Vp [m/s] | Thickness [m] | Density [kg/m$^3$] | Damping [%] |
|---|---|---|---|---|---|
| 1 | 248 | 1492 | 25 | 1730 | 1.01 |
| 2 | 274 | 1504 | 11 | 1750 | 0.91 |
| 3 | 407 | 1519 | 7 | 1830 | 0.61 |
| 4 | 563 | 1529 | 55 | 1900 | 0.44 |
| 5 | 665 | 1894 | 34 | 1950 | 0.38 |
| 6 | 702 | 2373 | 211 | 1960 | 0.36 |
| 7 | 837 | 2815 | 115 | 2010 | 0.3 |
| 8 | 844 | 2846 | 82 | 2020 | 0.3 |
| 9 | 1051 | 2846 | 84 | 2090 | 0.24 |
| 10 | 1363 | 3051 | 212 | 2180 | 0.18 |
| 11 | 1502 | 3051 | 51 | 2220 | 0.17 |
| 12 | 1705 | 3087 | 265 | 2270 | 0.15 |
| 13 | 1914 | 3751 | 237 | 2330 | 0.13 |
| 14 | 1942 | 3846 | 274 | 2330 | 0.13 |
| 15 | 2061 | 3942 | 124 | 2360 | 0.12 |
| 16 | 2111 | 4008 | 245 | 2370 | 0.12 |
| 17 | 2120 | 4063 | 653 | 2380 | 0.12 |
| 18 | 2672 | 4796 | 629 | 2500 | 0.09 |
| 19 | 2893 | 5124 | 1728 | 2540 | 0.09 |
| 20 | 3400 | 6000 | - | 2640 | 0.07 |

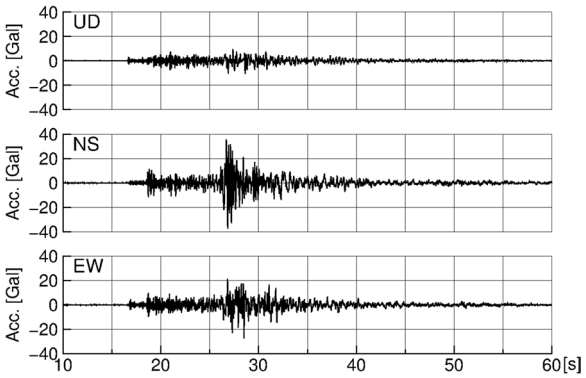


**Fig. 5** Observed motions of the target earthquake of step 2 at EEB. Time "10" corresponds to 03:03:10

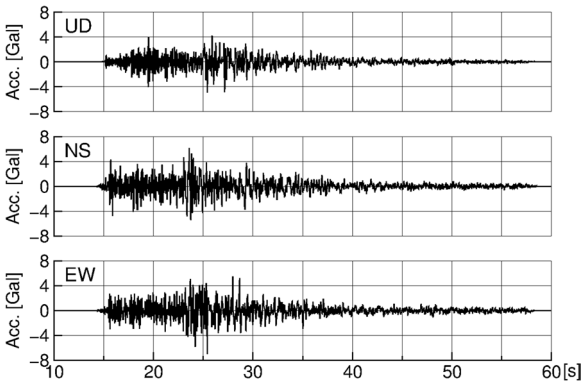


**Fig. 6** Estimated outcrop motions at the seismic bedrock of the target earthquake of step 2. Time "10" corresponds to 03:03:10

in a frequency range lower than 20 Hz. The predicted acceleration and velocity waveforms and the acceleration spectral amplitudes are shown in Fig. 7. The acceleration waveform was integrated within the frequency band from 0.1 to 20 Hz to obtain the velocity waveform. The actual records of the target earthquake at KUMA, which is the correct answer to the blind prediction exercise but was not released at the time of analysis, are also plotted in Fig. 7. The time shift of waveforms due to the wave propagation was not calculated automatically in the estimation process based on DFCe. Thus, it was manually calculated considering linear wave propagation of body wave from the surface to the bedrock at EEB and from EEB to KUMA via the epicentral distance. Vs and Vp structures inverted at EEB were used to calculate the time shifts from the surface to the seismic bedrock of the horizontal and vertical components, and the velocities of the seismic bedrock (Vs = 3400 m/s and Vp = 6000 m/s) were used to calculate the time shifts from the seismic bedrock at EEB to the seismic bedrock at KUMA via the epicentral distance. The spectral amplitudes were smoothed using the

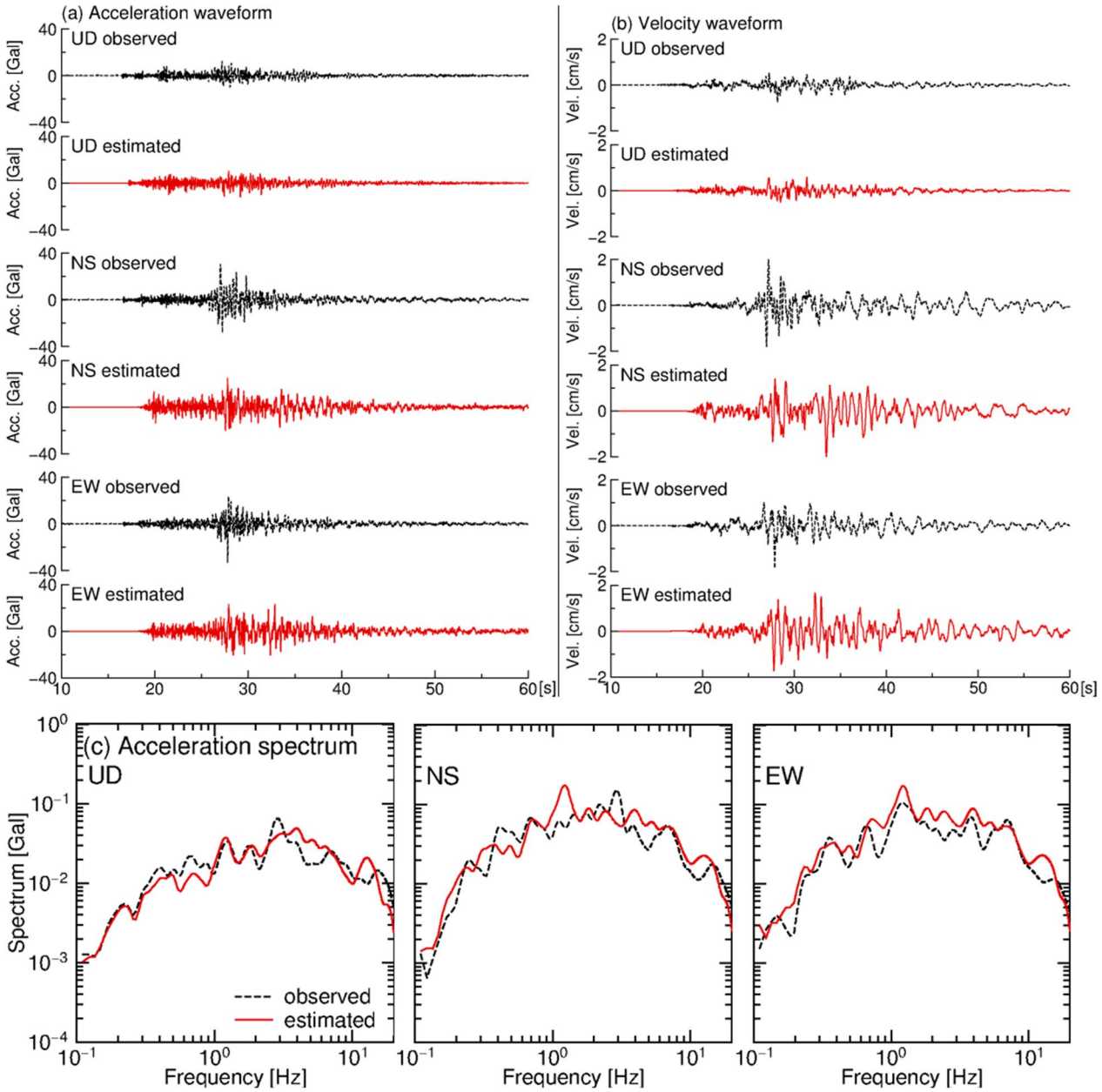


**Fig. 7** Predicted motions of the target earthquake of step 2 on the ground surface at KUMA. Dashed black lines are the observed motions at KUMA and solid red lines are the predicted motions. Time "10" corresponds to 03:03:10

logarithmic scale smoothing function with b = 30 (Konno and Ohmachi 1998) to remove the ripples of the spectra and compare their outlines.

The detailed phases of the predicted waveforms did not match the observed phases, but the general envelope shapes were similar. The spectral amplitudes of the predicted NS and EW components were the same because the spectral amplitudes of the input waves and the horizontal amplification factors, which were calculated from the Vs structure, were in common for the NS and EW components, and prediction analysis was performed in the frequency domain. The spectral levels of the horizontal and vertical components of the predicted waves at KUMA corresponded well with the observed waves, although they were estimated from the UD component of EEB.

The proposed method was applied to three earthquake events recorded at both KUMA and EEB for validation

purposes. Comparisons of the ground motion observed at KUMA and the estimated motions from EEB using the proposed method are shown in Additional file 1. The velocity was calculated from the acceleration by the integration in the frequency domain within the frequency band from 0.1 to 20 Hz. The envelopes of the estimated waveforms are similar to those observed. The estimated acceleration and velocity waveforms arrived slightly later (0.6 s) than those of the observations. There are several possible causes for this delay. The velocity structures at KUMA and EEB were identified in terms of the amplification factors, but were not well identified in terms of travel time. The travel time from EEB to KUMA via the epicentral distance was calculated assuming a homogeneous medium. Thus, the velocity structure below the seismic bedrock can be tuned. The spectral amplitudes of the estimated motions were also the same as those observed. However, the estimated amplitude was larger (approximately twice) than that observed between 3 and 7 Hz for all earthquakes. This discrepancy might be due to the site amplification factors at KUMA and EEB. The horizontal and vertical site amplification factors at EEB need to have a larger amplitude in that frequency range than the amplification factors in this study, or the horizontal and vertical site amplification factors at KUMA need to have smaller amplitudes than the amplification factors in this study. Further investigations of the arrival delay and discrepancy in amplitude are, thus, necessary.

### Prediction of the foreshock and mainshock of the 2016 Kumamoto earthquake

The ground motions at the KUMA during the foreshock and mainshock of the 2016 Kumamoto earthquake were predicted in Step 3 of the blind prediction exercise. These ground motions were predicted using the same procedure as in Step 2; however, an equivalent linear analysis was adopted to perform the one-dimensional soil-response analysis considering the nonlinear site response at KUMA during strong shaking. As shown in Fig. 1, the distance between KUMA and EEB was smaller than the distance between the observation sites and fault models. As for the foreshock and mainshock, all the S-wave arrivals from different parts of the fault surface would contribute naturally to form the diffusive conditions, even though the hypocentral distance from the rupture initiation point was small. Thus, we assumed that the source and path terms of the foreshock and mainshock for KUMA and EEB were similar.

For the ground motion predictions of the foreshock and mainshock, the seismic bedrock motions were estimated at EEB based on DFCe, assuming the generation of a diffuse field during strong shaking. Again, linearity of the vertical amplification factor during strong shaking was assumed. The nonlinearity is site dependent, and there was no reference for the vertical linearity investigated around the target site. Thus, the nonlinearity of the surface-to-borehole spectral ratio (SBR) was investigated at KMMH16, which is the closest KiK-net site to KUMA and EEB, but for reference. The distance from KMMH16 to KUMA is 12.5 km. Please see Additional file 1 for further details. The horizontal SBRs of the strong motions were smaller than the average of the weak motions in the high-frequency range. However, the vertical SBRs of strong motions were almost the same as the average of weak motions, even when the PGA of the vertical component was larger than 1000 cm/s (Gal). KMMH16 is far from KUMA and EEB but on the same plain; thus, the nonlinearity at KMMH16 is comparable to that at KUMA and EEB. The PGAs of the UD components of the foreshock and mainshock at EEB were 261 and 405 Gal, respectively. Thus, the vertical ground motions of the foreshock and mainshock were considered insufficient to cause large soil nonlinearity.

Based on these assumptions, the right-hand term of Eq. 2 was calculated linearly without the dynamic deformation characteristics of the soil (Nagashima and Kawase 2022). The spectral amplitudes of the three components of the seismic bedrock motion at EEB were estimated from the vertical motion observed on the surface at EEB. The horizontal components were estimated using Eq. 2. The vertical component was estimated by conventional deconvolution analysis, as performed in Step 2. These spectral amplitudes were then combined with the spectral phase of the observed motion at EEB to estimate the seismic bedrock motion. The unexpected vibration before P-wave arrival was tapered. The time shift due to the wave propagation through the subsurface structure should be estimated considering the soil nonlinearity. However, the procedure based on DFCe does not use nonlinear properties. Hence, the time shift can be estimated by assuming only a linear soil response. As a result, the estimated time shift is shorter than the actual time shift, and the arrival times of the estimated bedrock motion and the predicted motion at KUMA are later than the actual arrival times because of the insufficient correction relative to the real nonlinear time shift.

The acceleration waveforms of the foreshock and aftershock observed at EEB are shown in Figs. 8 and 9, respectively. Figures 10 and 11 show the estimated outcrop motions of the foreshock and mainshock, respectively, at the seismic bedrock level. The PGAs of the estimated horizontal bedrock motions were approximately one-fifth of those observed on the ground surface, and the PGAs of the vertical bedrock motions were approximately two-fifths of those observed on the ground surface.

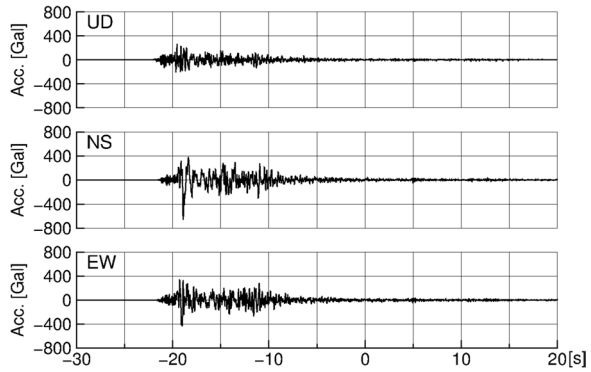


**Fig. 8** Observed foreshock at EEB. Time "− 30" is corresponding to 21:26:30

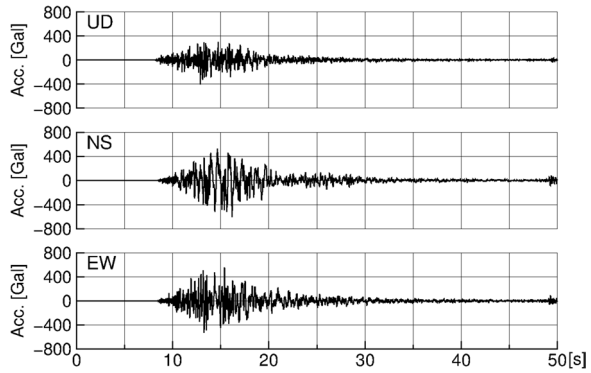


**Fig. 9** Observed mainshock at EEB. Time "0" is corresponding to 01:25:00

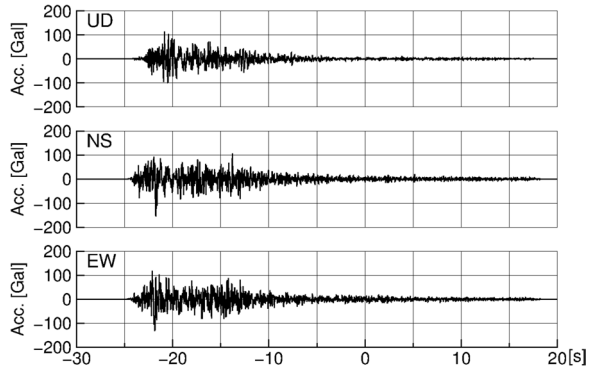


**Fig. 10** Estimated outcrop motions at the seismic bedrock of EEB during the foreshock. Time "− 30" corresponds to 21:26:30

Using the estimated bedrock waves at EEB, the identified velocity structure at KUMA and the dynamic deformation characteristics ($G/G_0$-γ and h-γ relationships; Matsushima et al. 2021, 2023), the equivalent linear analysis was performed by DYNEQ (Yoshida 2020) to predict the ground motions on the surface at KUMA. The

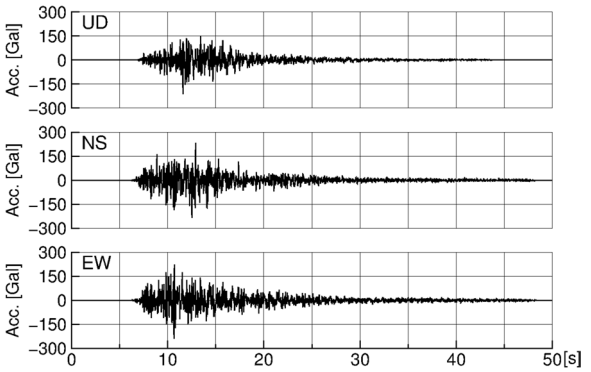


**Fig. 11** Estimated outcrop motions at the seismic bedrock of EEB during the mainshock. Time "0" corresponds to 01:25:00

dynamic deformation characteristics distributed by the ESG6 blind prediction committee were obtained from the undisturbed soil specimen samples at the target site. Specimens of sandy silt, clay with sand, sand, sand with silt, and silt with sand were obtained at depths of 4, 8, 13, 20, and 23 m and named T-1, T-2, Tr-3, Tr-4, and T-5, respectively. The dynamic deformation characteristics of the gravel were not distributed; therefore, the common characteristics of Imazu and Fukutake (1986) were adopted. These characteristics were used for the velocity layers by referring to the boring logs distributed by the organizer at the target site. The details of the velocity structure and assignment of the dynamic deformation characteristics are listed in Table 5. According to the distributed boring log data, sand with silt and sand with gravel layers exist at depths between 24.79 and 30.9 m, but no laboratory test has been performed to sample them at this depth; thus, the dynamic deformation characteristics of Tr-4, which had one of the deepest sandy soils in the distributed data, was used for this depth. A linear response was assumed for layers below the 4th layer. In this analysis, the damping depended on the frequency, $h = h_0 * f^{-1}$, where $h_0$ is the damping obtained using the h-γ relationship. As aforementioned, the vertical component was predicted using linear soil-response analysis.

The predicted results for the foreshock and mainshock are shown in Figs. 12 and 13, respectively. The observed data for the foreshock and mainshock at KUMA, which were not released at the time of analysis, are also plotted in Figs. 12 and 13. Velocity waveforms were obtained by integrating acceleration waveforms in the frequency domain between 0.1 and 20 Hz. The spectra were smoothed using a logarithmic scale smoothing function with b of 30. In both cases of the foreshock and the mainshock, the resultant effective strains were less than 0.5% for most of the layers, as shown in Figs. 12e and 13e. The

**Table 5** Assignment of dynamic deformation characteristics

| No. | Vs[m/s] | Vp[m/s] | H[m] | Depth[m] | Number of elements | Dynamic deformation characteristics |
|---|---|---|---|---|---|---|
| 1 | 153 | 1301 | 8 | 8 | 3 | T-1 |
| | | | 2 | 10 | 1 | T-2 |
| | | | 10 | 20 | 4 | Tr-3 |
| | | | 3 | 23 | 2 | Tr-4 |
| | | | 3 | 26 | 2 | T-5 |
| 2 | 229 | 1301 | 5 | 31 | 10 | Tr-4 |
| | | | 4 | 35 | 10 | Gravel |
| 3 | 284 | 1301 | 3 | 38 | 10 | Gravel |
| | | | 28 | 66 | 10 | Linear |
| 4 | 541 | 1562 | 18 | 84 | 10 | Linear |

maximum effective strain was 1.06% at a 20 m depth of the NS component during the mainshock, but the effective strains of other layers were less than 1%, which is considered to be the maximum value of the available effective strain, and the exceedance from the available strain level is slight; thus the equivalent linear analysis is considered valid. The strain is concentrated at a depth of approximately 20 m, where the boundary between Tr-3 and Tr-4 is located. The nonlinear behavior of the velocity structure during the foreshock was similar to that during the mainshock. Sun et al. (2020) estimated ground motions during the mainshock of the 2016 Kumamoto earthquake in Mashiki downtown area, where was heavily damaged by the earthquake, using the equivalent linear analysis. The resultant maximum strain at KMMH16 was smaller than 0.25%. Satoh et al. (1995) performed the equivalent linear analysis at a site in Ashigara valley and resulted the maximum effective strain of 0.2%. Régnier et al. (2016) conducted the PRENOLIN project and collected equivalent linear/nonlinear simulation results at Japanese sites. The resultant maximum strains estimated for high-frequency content input motion were smaller than 0.3% and those for low-frequency content input motion were around 1%. The strain levels of our prediction are in the same order with these precious studies.

In Figs. 12d and 13d, the horizontal amplification factors in the cases of equivalent linear analysis were smaller than the linear amplification factor, especially from 0.4 Hz to 5 Hz (resultant amplification factors were approximately 60% of the linear amplification factor on average between 0.4 and 5 Hz for both earthquakes) because of soil nonlinearity. The predicted accelerations of both earthquakes shown in Figs. 12a and 13a are almost similar but contain more high-frequency components than the observed acceleration waveforms. However, the predicted velocities shown in Figs. 12b and 13b are smaller than the observed velocities. These discrepancies were also observed when comparing the spectra (Figs. 12c and 13c). The spectral levels of the horizontal components of the foreshock and the mainshock were comparable to that of the observed motions, but the spectral level of the predicted motions tended to be smaller at 1 Hz and 0.5 Hz than that of the observed motions (the averaged ratios of the predicted over observed spectra are approximately 0.41 between 0.7 and 1.2 Hz and 0.42 between 0.3 and 0.9 Hz), respectively, and larger at 10 Hz than the observed ones (the averaged ratios are approximately 2.4 between 8.0 and 19.0 Hz and 2.2 between 8.0 and 18.0 Hz). The predicted spectral amplitudes of the UD component reproduced the observed amplitudes for the foreshock and mainshock. In Figs. 12a, b, 13a, b, the peak amplitude arrived later than the observed amplitude because the time shift of the input waves was calculated assuming a linear response of the subsurface structure. Another possible reason for the difference in phase is that the identified velocity structures were not optimized for travel times and that the estimation method based on DFCe modifies the spectral amplitude but not the phase.

The difference in the spectral amplitude shown in the low-frequency range may have resulted from the difference in the horizontal and vertical components at EEB. Thus, in the main coherent S-wave portion, the energy partition ratio of the horizontal and vertical components does not converge yet and is too strong to construct sufficiently diffused wave field characteristics. In avoiding such a coherent nature of the ballistic waves directly from the source, a possible method is to estimate the horizontal site amplification factor at reference site EEB considering soil nonlinearity, and then deconvolve the observed motions by the amplification factor to estimate the bedrock wave. The site amplification factor can be estimated directly from the observed horizontal and

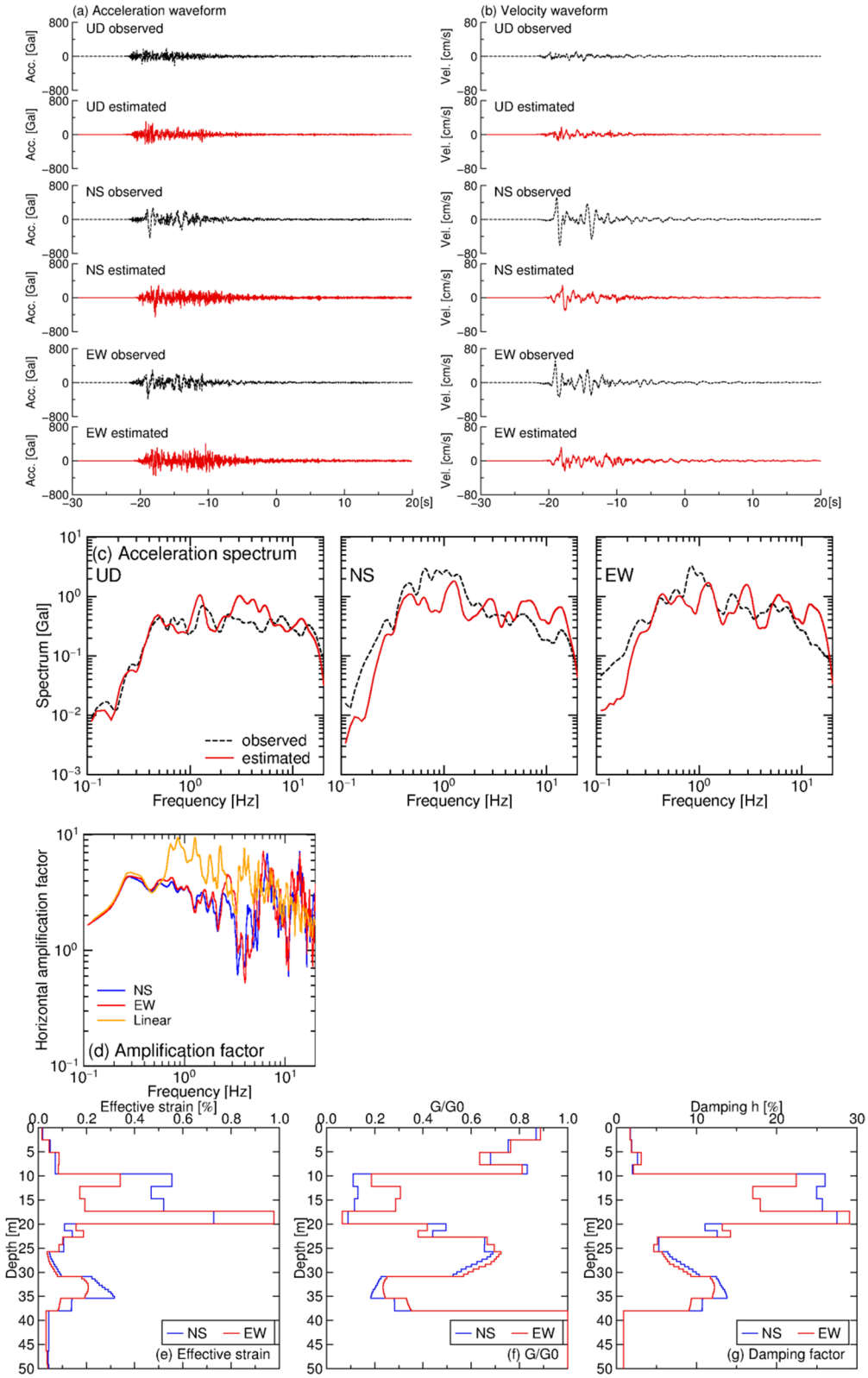


**Fig. 12** Estimated motions at KUMA for the foreshock and the resultant strain and dynamic deformation characteristics. **a**, **b** and **c** Show comparisons of the observed ground motions at KUMA and the predicted motions; dashed black lines are the observed motions at KUMA and solid red lines are the predicted motions. Time "− 30" is corresponding to 21:26:30. **d** Shows horizontal amplification factors at KUMA estimated by linear and equivalent linear analyses. **e**, **f** and **g** Show depth distributions of effective strain, $G/G_0$ and damping, respectively

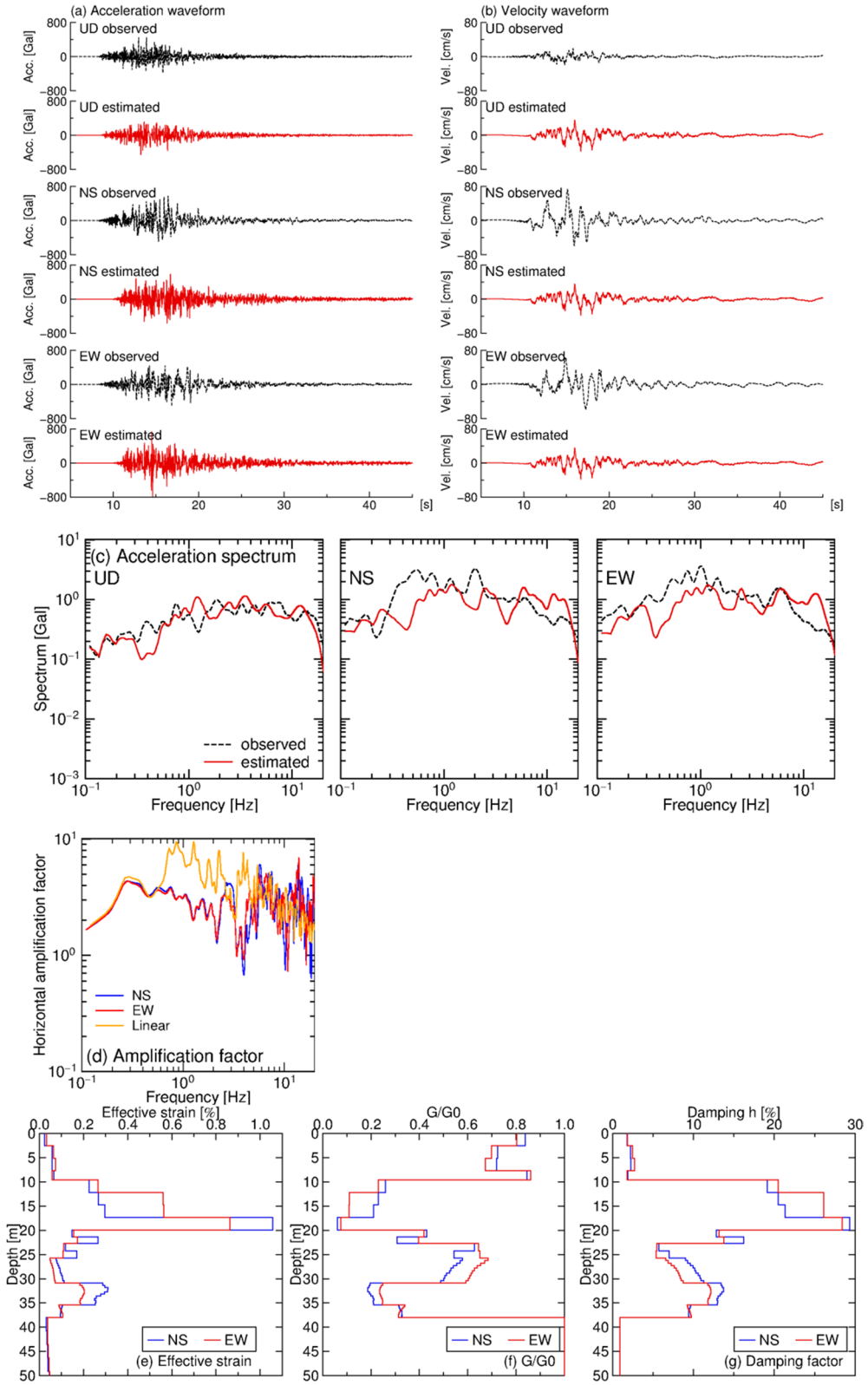


**Fig. 13** Estimated motions at KUMA for the mainshock and the resultant strain and dynamic deformation characteristics. **a**, **b** and **c** Show comparisons of the observed ground motions at KUMA and the predicted motions; dashed black lines are the observed motions at KUMA and solid red lines are the predicted motions. Time "10" is corresponding to 01:25:10. **d** Shows horizontal amplification factors at KUMA estimated by linear and equivalent linear analyses. **e**, **f** and **g** Show depth distributions of effective strain, $G/G_0$ and damping, respectively

vertical motions on the ground surface without dynamic deformation parameters based on DFCe (Nagashima and Kawase 2022), as shown in Eq. 3:

$$\left|\mathrm{TF}_{\mathrm{horizontal}}(\mathrm{f})\right| = \frac{\mathrm{H(f)}}{\mathrm{V(f)}}\sqrt{\frac{\alpha}{\beta}}\left|\mathrm{TF}_{\mathrm{vertical}}(\mathrm{f})\right|. \quad (3)$$

Assuming the linearity of the vertical amplification factor during strong shaking, we obtained the horizontal site amplification factor ($|\mathrm{TF}_{\mathrm{horizontal}}(\mathrm{f})|$) from the observed surface motions (H(f) and V(f)) and the vertical site amplification factor ($|\mathrm{TF}_{\mathrm{vertical}}(\mathrm{f})|$). In applying this method, a time window that satisfies the same degree of nonlinearity as the main S-wave but does not have the coherent nature of the ballistic waves included in the main S-wave is required. Equation 3 was available after a detailed investigation of the observed waveforms; thus, we did not select this method for the blind prediction exercise.

The difference in the spectral amplitudes in the high-frequency range is mainly controlled by the damping factors in the equivalent linear analysis. The damping factor depends on the h-γ relationship, for which a frequency dependence with an exponent of − 1 was assumed in this study. Tuning these parameters would improve the matching of the spectral amplitude in the high-frequency range.

To estimate the seismic bedrock motion, we assumed the linearity of the vertical amplification factor and the establishment of DFCe. In theory, these assumptions have been proven phenomenologically but not completely. Therefore, further investigation of these assumptions is necessary.

## Conclusion

We participated in a blind prediction exercise organized by the ESG6 blind prediction committee and predicted ground motions during one small aftershock, the foreshock, and the mainshock of the 2016 Kumamoto earthquake by using the bedrock motion estimation method based on DFCe. First, the subsurface velocity structures at KUMA, the target site of the blind prediction exercise, and those at EEB, our reference site for estimating bedrock motion, were inverted from the EHVRs. Assuming the generation of a diffuse field during a single earthquake and linearity of the vertical amplification factor during strong shaking for the foreshock and mainshock, we estimated the spectral amplitudes of the bedrock motions from the vertical motions observed on the ground surface and the P-wave velocity structure at EEB. The bedrock motions were obtained by combining the estimated spectral amplitude and the spectral phase of the observed records. Finally, earthquake motions on the ground surface at KUMA were predicted using linear and equivalent linear analyses. The spectral levels of the predicted motions corresponded to the observed motions, although the spectral amplitudes of both the horizontal and vertical components of the bedrock motions were estimated from the vertical components at EEB. The phases of the predicted motions did not correspond to the observed waves. One possible reason for this phase difference is that the estimation method based on DFCe does not control the spectral phase. Another notable discrepancy is the gap in the spectral amplitude at intermediate- and high-frequency ranges, which may be due to the insufficient diffused field causing the instability of the horizontal and vertical energy partition ratios or due to the setting of damping parameters in the equivalent linear analysis. The potential of the proposed method for estimating seismic ground motions at a target site was clearly demonstrated in this exercise.

### Abbreviations

| | |
|---|---|
| ESG | Effect of Surface Geology on seismic motion |
| DFCe | Diffuse Field Concept for earthquake |
| EHVR | Horizontal-to-Vertical spectral Ratio of earthquake |
| JMA | Japan Meteorological Agency |
| NS | North–South component |
| EW | East–West component |
| UD | Up-Down component |
| Vs | S-wave velocity |
| Vp | P-wave velocity |
| HHS | Hybrid Heuristic Searching method |
| RMS | Root mean square value calculated from two horizontal components |
| PGA | Peak ground acceleration |
| SBR | Surface-to-borehole spectral ratio |

## Supplementary Information

The online version contains supplementary material available at https://doi.org/10.1186/s40623-023-01859-8.

**Additional file 1:** Velocity, EHVR, and SAF comparisons.

### Acknowledgements

The collection and distribution of the data for the blind prediction by the ESG6 local organizing committee is highly appreciated. The observation and publication of earthquake records by Japan Meteorological Agency is also highly appreciated. We highly appreciate the insightful reviewers comments. We would like to thank Editage (www.editage.com) for English language editing.

### Author contributions

FN: analyzing data, EHVR inversion, and nonlinear synthesis. HK: strategic planning and advice on the interpretation. EI: discussing the interpretation of the results. KN: evaluation of the site amplification at EEB.

### Funding

A part of this study was supported by the JSPS Grand-in-Aid (Kaken-hi) for Basic Research (B) No. 19H02405. Support for the laboratory of Sophisticated Earthquake Risk Evaluation from Hanshin Consultants Co. Ltd. is highly appreciated.

### Availability of data and materials

Earthquake records at KUMA were provided by the ESG6 blind prediction committee only to the blind prediction participants. Earthquake records at EEB

are distributed by Japan Meteorological Business Support Center (http://www.jmbsc.or.jp/jp/offline/cd0220.html). Ground motions of the foreshock and the mainshock of the 2016 Kumamoto earthquake at EEB were obtained from the JMA website (https://www.data.jma.go.jp/svd/eqev/data/kyoshin/jishin/160416 0125_kumamoto/index.html, Accessed in 27 Oct 2020). Boring log data and dynamic deformation characteristics were reported in Matsushima et al. (2021, 2023) as a part of the activities of the ESG6 blind prediction committee.

## Declarations

### Ethics approval and consent to participate

We all have checked and approved.

### Consent for publication

All authors have agreed to the publication of the manuscript.

### Competing interests

The authors declare that they have no competing interests.

### Author details

[1]Disaster Prevention Research Institute, Kyoto University, Gokasho, Uji, Kyoto, Japan. [2]HAZAMA ANDO CORPORATION, Tsukuba, Ibaraki, Japan.

Received: 6 October 2022 Accepted: 10 June 2023
Published online: 25 June 2023

### References

Asten MW, Yong A, Foti S, Hayashi K, Martin AJ, Stephenson WJ, Cassidy JF, Coleman J, Nigbor R, Castellaro S, Chimoto K, Cornou C, Cho I, Hayashida T, Hobiger M, Kuo CH, Macau A, Mercerat ED, Molnar S, Pananont P, Pilz M, Poovarodom N, Saez E, Wathelet M, Yamanaka H, Yokoi T, Zhao D (2022) An assessment of uncertainties in VS profiles obtained from microtremor observations in the phased 2018 COSMOS blind trials. J Seismol 26:757–780

Bard PY, SESAME participants (2004) The SESAME project: an overview and main results. In: Proceedings of the 13th World Conference in Earthquake Engineering, Vancouver, 1–6 August, 2004, 2207

Chiara S, Roberto P, Marco S (2011) Comparison of 3D, 2D and 1D numerical approaches to predict long period earthquake ground motion in the Gubbio plain. Central Italy Bull Earthq Eng 9(6):2007–2029

Chimoto K, Yamanaka H, Tsuno S, Shigefuji M, Kanno T, Sato H, Higashi S, Shinoyama D, Yoshimi M, Sugiyama T, Takai N, Matsushima S, Nagashima F, Kawase H, Hayakawa T, Uetake T, Senna S, Inagaki Y, Hayashida T, Oji S (2021) Results of blind prediction Step 1: subsurface velocity structure model of Kumamoto Test Site. In: Proceedings of the 6th IASPEI/IAEE international symposium on effects of surface geology on seismic motion, Uji, Japan, 31 August-2 September 2021, SS102-BP1

Chimoto K, Yamanaka H, Tsuno S, Matsushima S (2023) Predicted results of the velocity structure at the target site of the blind prediction exercise from microtremors and surface wave method as Step-1, -report for the experiments for the 6th international symposium on effects of surface geology on seismic motion. Earth Planets Space. https://doi.org/10.1186/s40623-023-01842-3

Cornou C, Ohrnberger M, Boore DM., Kudo K, Bard PY (2006) Derivation of structural models from ambient vibration array recordings: results from an international blind test. In: Proceedings of the 3rd International Symposium on the Effects of Surface Geology on Seismic Motion, Grenoble, France, NBT

Fukutake K, Ohtsuki A, Sato M, Shamoto Y (1990) Analysis of saturated dense sand-structure system and comparison with results from shaking table test. Earthq Eng Struct Dyn 19(7):977–992

Giuseppe DG, Iolanda G, Fabrizio C, Giuliano M, Marco T (2014) Shear-wave velocity profile and seismic input derived from ambient vibration array measurements: the case study of downtown L'Aquila. Geophys J Int 198(2):848–866

Graves R, Pitarka A (2016) Kinematic ground motion simulations on rough faults including effects of 3D Stochastic velocity perturbations. Bull Seismol Soc Am 106(5):2136–2153

Imazu M, Fukutake K (1986) Dynamic shear modulus and damping of gravel materials. In: Proceedings of the 21th annual meeting of the Japanese Geotechnical Society, Sapporo, Japan, 1986, 509–512

Irikura K, Miyake H (2011) Recipe for predicting strong ground motion from crustal earthquake scenarios. Pure Appl Geophys 168:85–104

Kawase H, Sánchez-Sesma FJ, Matsushima S (2011) The optimal use of horizontal-to-vertical spectral ratios of earthquake motions for velocity inversions based on diffuse-field theory for plane waves. Bull Seismol Soc Am 101(5):2001–2014

Kobayashi K, Abe Y, Uetake T, Mashimo M, Kobayashi H (1995) Inversion of spectrum ratio of Horizontal to Vertical component of preliminary tremors. Summ Tech Papers Ann Meeting Arch Inst Japan 1995:307–308

Konno K, Ohmachi T (1998) Ground-motion characteristics estimated from spectral ratio between horizontal and vertical components of microtremor. Bull Seismol Soc Am 88(1):228–241

Matsushima S, Hirokawa T, Martin FD, Kawase H, Sánchez-Sesma FJ (2014) The effect of lateral heterogeneity on horizontal-to-vertical spectral ratio of microtremors inferred from observation and synthetics. Bull Seismol Soc Am 104(1):381–393

Matsushima S, Yamanaka H, Tsuno S, Sato H, Inagaki Y (2021) Results of borehole survey at the target site of ESG6 blind prediction exercise and laboratory tests. In: Proceedings of the 6th IASPEI/IAEE international symposium: Effects of Surface Geology on seismic motion, Uji, Japan, 31 August-2 September 2021, SS101

Matsushima S, Yamanaka H, Tsuno S, Chimoto K, Suzuki H, Kawase H (2023) Investigation of the subsurface structure at the target site in Kumamoto, Japan and the distributed data of the blind prediction exercise, Report for the experiments for "The 6th International Symposium on Effects of Surface Geology on Seismic Motion". Earth Planets Space (under revision)

Nagashima F, Matsushima S, Kawase H, Sánchez-Sesma FJ, Hayakawa T, Satoh T, Oshima M (2014) Application of horizontal-to-vertical (H/V) spectral ratios of earthquake ground motions to identify subsurface structures at and around the K-NET site in Tohoku. Japan Bull Seismol Soc Am 104(5):2288–2302

Nagashima F, Kawase H (2022) Estimation of horizontal amplification factor and incident spectrum at Seismic bedrock during strong shaking based on diffuse field concept. J Japan Assoc Earthquake Eng 22(2):217–236

Régnier J, Bonilla LF, Bard PY, Bertrand E, Hollender F, Kawase H, Sicilia D, Arduino P, Amorosi A, Asimaki D, Boldini D, Chen L, Chiaradonna A, Martin FD, Ebrille M, Elgamal A, Falcone G, Foerster E, Foti S, Garini E, Gazetas G, Gelis C, Ghofrani A, Giannakou A, Gingery JR, Glinsky N, Harmon J, Hashash Y, Iai S, Jeremic B, Kramer S, Kontoe S, Kristek J, Lanzo G, DiLernia A, Lopez-Caballero F, Marot M, McAllister G, Mercerat ED, Moczo P, Montoya-Noguera S, Musgrove M, Nieto-Ferro A, Pagliaroli A, Pisano F, Richterova A, Sajana S, Santisi-d'Avila MP, Shi J, Silvestri F, Taiebat M, Tropeano G, Verrucci L, Watanabe K (2016) International benchmark on numerical simulations for 1D, nonlinear site response (PRENOLIN): verification phase based on canonical cases. Bull Seismol Soc Am 106(5):2112–2135

Régnier J, Bonilla LF, Bard PY, Bertrand E, Hollender F, Kawase H, Sicilia D, Arduino P, Amorosi A, Asimaki D, Boldini D, Chen L, Chiaradonna A, Martin FD, Elgamal A, Falcone G, Foerster E, Foti S, Garini E, Gazetas G, Gelis C, Ghofrani A, Giannakou A, Gingery J, Glinsky N, Harmon J, Hashash Y, Iai S, Kramer S, Kontoe S, Kristek J, Lanzo G, DiLernia A, Lopez-Caballero F, Marot M, McAllister G, Mercerat ED, Moczo P, Montoya-Noguera S, Musgrove M, Nieto-Ferro A, Pagliaroli A, Passeri F, Richterova A, Sajana S, Santisi-d'Avila MP, Shi J, Silvestri F, Taiebat M, Tropeano G, Vandeputte D, Verrucci L (2018) PRENOLIN: international benchmark on 1D nonlinear site-response analysis -validation phase exercise. Bull Seismol Soc Am 108(2):876–900

Satoh T, Sato T, Kawase H (1995) Nonlinear behavior of soil sediments identified by using Borehole Records observed at the Ashigara Valley. Japan Bull Seismol Soc Am 85(6):1821–1834

Senna S, Wakai A, Suzuki H, Yatagai A, Matsuyama H, Fujiwara H (2018) Modeling of the subsurface structure from the seismic bedrock to the ground surface for a broadband strong motion evaluation in Kumamoto Plain. J Disaster Res 13(5):917–927

Sun J, Nagashima F, Kawase H, Matsushima S (2020) Site effects analysis of shallow subsurface structures at Mashiki town, Kumamoto, based on

microtremor horizontal-to-vertical pectral ratios. Bull Seismol Soc Am 110(6):2912–2938
Tsuno S, Kawase H, Yamanka H, Matsushima S, Iwata T, Hayakawa T, Ikeura T, Noguchi S, Kaneda K (2021a) Results of blind prediction Step 2: simulation of weak motions observed at the Kumamoto test site. In: Proceedings of the 6th IASPEI/IAEE international symposium: Effects of Surface Geology on seismic motion, Uji, Japan, 31 August-2 September 2021a, SS103-BP3
Tsuno S, Kawase H, Yamanka H, Matsushima S, Iwata T, Hayakawa T, Ikeura T, Noguchi S, Kaneda K (2021b) Results of blind prediction Step 3: simulation of strong motions observed at the Kumamoto test site. In: Proceedings of the 6th IASPEI/IAEE international Symposium: Effects of Surface Geology on seismic motion, Uji, Japan, 31 August-2 September 2021b, SS103-BP3
Tsuno S, Nagashima F, Kawase H, Yamanaka H, Matsushima S (2023) Predicted results of the weak and strong ground motions at the target site of the blind prediction exercise as Step 2 and Step-3, -Report of the experiments for "The 6th International Symposium on Effects of Surface Geology on Seismic Motion". Earth Planets Space (under revision)
Yamanaka H (2007) Inversion of surface-wave phase velocity using hybrid heuristic search method. BUTSURI-TANSA 60(3):265–275
Yoshida N (2020) DYNEQ A computer program for DYNamic response analysis of level ground by EQuivalent linear method, Version 4.00. Kanto Gakuin University

## Publisher's Note